Engineering Structures 86 (2015) 84–98

Contents lists available at ScienceDirect

Engineering Structures

journal homepage: www.elsevier.com/locate/engstruct

Assessment of static rope behavior with asymmetric damage distribution

Juan Felipe Beltrán [a,*], Enzo De Vico [b]

[a] Dept. of Civil Engineering, University of Chile, Blanco Encalada # 2002 Of. 440, Santiago, Chile
[b] Dept. of Civil Engineering, University of Chile, Blanco Encalada # 2002, Santiago, Chile

ARTICLE INFO

Article history:
Received 8 February 2014
Revised 7 November 2014
Accepted 12 December 2014
Available online 12 January 2015

Keywords:
Damaged synthetic-fiber rope
Analytical model
Rope failure
Asymmetric damage

ABSTRACT

In this paper, a mechanical model is proposed to estimate the static response (stiffness, residual capacity, deformed configuration, strain/strain distribution within cross-section, and deformation capacity) of a rope asymmetrically damaged. In this study, damage corresponds to the complete rupture of one or more rope components in a particular rope cross-section location. In the proposed model, the damaged rope is assumed to behave as a nonlinear beam under biaxial bending and axial load with Bernoulli's kinematic hypothesis. Biaxial bending arises from the unbalanced radial contact forces within rope cross-section, which are related to the initial helical geometry configuration of the rope components, due to the asymmetric damage distribution. An efficient and robust iterative cross-sectional numerical algorithm is implemented to estimate the asymmetric damaged rope capacity curve, stress and strain distributions throughout rope cross-section and rope geometry deformation for a prescribed axial displacement of the rope. The results given by the proposed model are found to be in good agreement with available static tension tests on asymmetrically damaged small-scale (ropes diameter equal to 6 mm) polyester ropes and their corresponding 3D finite element (FE) simulations with lower computational cost. Additionally, compared to the solutions obtained by previous analytical models reported in the literature, the range of applicability associated to the degree of damage to rope cross-section (number of broken rope components) is extended.

1. Introduction

Ropes are employed in many engineering applications including cranes, lifts, mine hoisting, bridges, cableways, electrical conductors, offshore mooring systems and so on. This wide range of usage demands ropes manufactures to provide different configurations of ropes suited for different purposes, having a different number and arrangement of rope components within the rope cross-section, and rope components can be made of different materials such as metal, natural and synthetic fibers [1,2].

Mechanical demands, abrasion, and environmental interaction (corrosion, ultra-violet light, chemical, and heat exposures, etc.) degrade the properties of the individual rope components continuously during rope operational service. This degradation process, that represents how damage in a rope evolves, could result in the complete rupture of one of more rope component and eventually will lead to rope failure. Damage to ropes, which could start during rope transportation and installation, is complex and different for each rope application, revealing the local operating parameters and the characteristics of the rope selected [3].

The understanding of the interaction of the factors that induce damage to rope and their dependence on the rope operational conditions are essential to estimate rope service life at the design stage and to establish the appropriate rope inspection methods and discard criteria. Hence, the service life of a rope can be greatly extended by following a planned program of installation, operation, maintenance, and inspection [3]. In this context, damage-tolerance property (i.e., the ability of a rope to withstand damage), is an essential parameter for rope design, rope evaluation during operational service, and for developing discard criteria according to rope usage based on the residual strength and deformation capacity that the damaged rope can sustain.

Several experimental [4–12] and theoretical [13–18] studies have shown that the impact of the presence of broken rope components on overall rope response (stiffness, residual strength and deformation capacity) depends on the length of the rope, number of broken rope components (degree of damage) and their distributions throughout rope cross-section (symmetric and asymmetric)

* Corresponding author.
E-mail addresses: jbeltran@ing.uchile.cl (J.F. Beltrán), enzodevico@gmail.com (E. De Vico).

http://dx.doi.org/10.1016/j.engstruct.2014.12.026
0141-0296/

and along the rope length, and rope construction. These studies have mainly been conducted on steel wire ropes and synthetic fiber ropes. In particular, if the rope length, type of rope construction, and location of the damaged cross-section are fixed, above studies conclude that the effect of rope components breaks on rope response is not always directly proportional to the equivalent loss of cross-sectional area (the so-called net area effect) and asymmetric damage distribution induces a lateral displacement of the rope and a non-uniform strain (and stress) distribution throughout rope cross-section, resulting in premature failure (deformation capacity) of the asymmetrically damaged rope relative to the intact rope. In addition, depending on the location of the broken components throughout damaged cross-section (inner or outer cross-section layers) potential strain localization around the failure region can develop due to the contact interaction among the unbroken and broken rope components, and as a result, a weaken cross-section acts over a localized region. The existence of this weaken cross-section can also cause the premature failure of rope components and reduce the rope failure strain and the maximum load a damaged rope is capable of resisting.

In this paper a simply mechanical model is proposed to estimate the deformed configuration, stress–strain distribution within cross-section and the capacity curve of an asymmetrically damaged rope subjected to axisymmetric loading conditions. This model assumes that an asymmetrically damaged rope behaves as a nonlinear beam under biaxial bending and axial load with Bernoulli's kinematic hypothesis neglecting the potential incremental contribution of broken rope components to overall rope response due to frictional forces (strain localization around the failure region effect) [16]. Comparisons with available static tension tests on asymmetrically damaged small-scale (ropes diameter equal to 6 mm) polyester (PET) ropes [10], previous analytical model reported in the literature [13,15], and 3D finite element (FE) simulations [18] are performed to validate the proposed model.

2. Numerical and analytical models

In this section, the main results presented in [18] are summarized in which 3D FE simulations (numerical models) were carried out to estimate the effect of asymmetric damage distribution to rope cross-section on rope response. The conclusions of these numerical simulations were used as the basis for developing a simplified and computational less expensive analytical model that allows predicting static behavior of asymmetric damaged rope, motivated by the computationally intensive 3D FE simulations. The formulation of this analytical model is presented in detail in this section.

2.1. Motivation: numerical models (FE simulations)

Beltran and Vargas [18] developed 3D FE models using the commercial software ANSYS for a particular PET rope component construction (hereafter referred as ropes) tested to failure (static capacity test) by Li et al. [10]: 6 mm diameter rope comprised of eight helical components (second layer of the rope) wound around a straight core (first layer of the rope), with initial pitch distance p_0 and helix angle θ_0 (angle between the longitudinal axis of the rope and local axis of the rope components) equal to 81 mm and 9.5° respectively. For modeling purpose, tested ropes geometry has one hierarchical structure identified (helical components wound around a central straight core) which defines the *level* of the rope geometry which in this case is one (i.e. one-level rope). These one-level two-layer ropes had initial lengths (L_0) equal to 610 mm (approximately $8p$) and they were damaged prior loading by cutting a prescribed number of rope components (degree of damage) at ropes midspan that were distributed symmetrically and asymmetrically within rope cross-sections.

The boundary conditions of each 3D FE model considered one end section of the rope fully clamped and at the other end an axial displacement history is specified and the cross-section is prevented from rotating. For the particular case of asymmetrically damaged ropes, 3D FE simulations demonstrated that these ropes deflect laterally inducing a non-uniform axial strain distribution throughout rope cross-sections and a reduction in their residual strengths and deformation capacities relative to the net area effect concept (model that just neglects the contribution to rope response of the broken components). In order to illustrate the above general conclusions (details can be found in [18]), the deformed configuration and axial strain (natural strain) distribution throughout rope cross-section and along the rope length for the rope W_{12} given by 3D FE simulations are depicted in Fig. 1. The notation used to identify a particular cross-section is as follows: W_{ij} where W refers to the cross-section and the indices i and j refer to the broken rope components (i and j vary from 0 to 9) based on the undamaged rope cross-section (W_u) also shown in the figure (Fig. 1a and b). The degree of asymmetry of the cross-section is quantified by a scalar quantity termed the index of asymmetry (IA), which captures the shift of the center of stiffness of the rope cross-section from its centroid due to the asymmetry of damage distribution as explained in Appendix A [18]. As the values of the parameter IA vary in a nonlinear fashion with respect to the rope axial strain due to the nonlinearity of the constitutive law of the PET rope components, its initial value, $(IA)_0$, is considered as a representative measure of the degree of asymmetry of the rope cross-section as discussed in [18].

To be consistent with previous researchers [10,11,17,18], measured and predicted damaged rope axial load-axial strain curves are plotted up to the maximum load and its corresponding strain, that represent the onset of damaged rope failure in which the subsequent fracture process of the rope cross-section is not part of this study. Consequently, these pairs of data are assumed to be the failure axial loads and failure axial strains of the analyzed ropes. This assumption is supported by several experimental and analytical research studies available in the literature ([11,19–22]) that conclude that after the rope reaches its maximum tensile, it experiences softening in a very small region of the plane axial load–strain in comparison to the region that the rope develops its maximum capacity.

Based on the results shown in Fig. 1c, the maximum axial strains are developed in the adjacent rope components to broken components (shown in gray color) and the minimum values are developed in the opposite rope components. Based on the conclusions drawn in [18], the gradient of the axial strain distribution throughout damaged rope cross-section increases as the $(IA)_0$ (hereafter referred as IA) value gets larger, in which the ratios between the maximum and minimum strain values at the onset of ropes failure, for example, are 1.15, 1.20 and 1.30 for ropes W_1, W_{12} (shown in Fig. 1c), and W_{1234}, respectively. As a reference, this ratio value for the case of an initially undamaged rope (W_u) is 1.11. Consequently, due to the increasing gradient in the axial strain distribution, an increasing additional reduction of the residual strength relative to the net area effect (reduction in rope strength is proportional to the loss of cross-sectional area) occurs while the deformation rope capacity (failure strain) decreases compared to the intact rope value: maximum additional reduction of the residual strength is close to 10% for rope W_{1234}; and for the same rope, 7% in reduction of failure axial strain value relative to the intact rope (Table 1).

For the particular rope construction studied in [18], unbroken rope components of an asymmetric damaged rope develop constant axial strain values along the ropes lengths which suggests

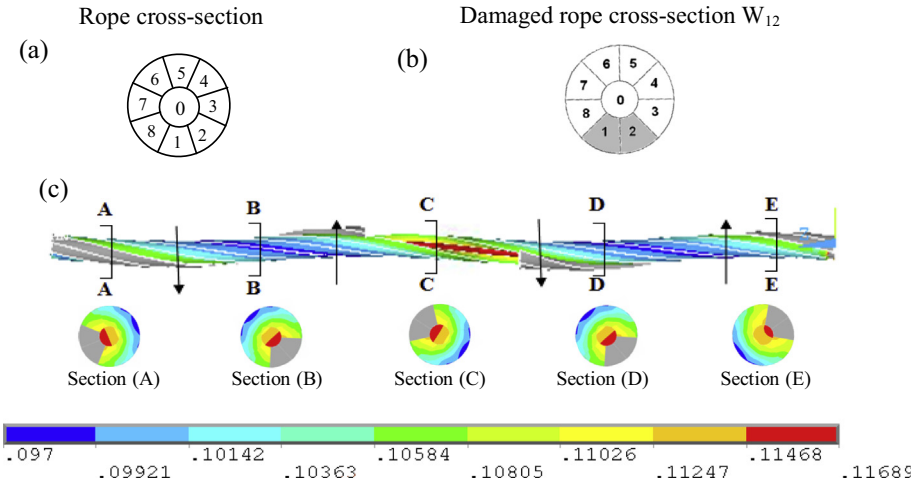

Fig. 1. (a) Rope cross-section and nomenclature of its components; (b) rope W_{12}; (c) Deformed configuration and strain distribution within rope cross-section and along rope length of rope W_{12} given by 3DFE simulation.

Table 1
Summary of the results given by the 3D FE simulations: asymmetric damaged ropes.

Rope	$(IA)_0$	Axial strain at failure		Residual strength (kN)			Lateral deflection (mm)	
		Exp. Data	3D FE model	Exp. Data	3D FE model	Net area effect model	$\varepsilon = 0.025$	$\varepsilon = 0.071$
W_u	0	0.115–0.127	0.117	22.3–25.6	23.5		–	–
W_{136}	0.093	0.097–0.114	0.115	12.2–17	15.6	15.7	0.23	0.27
W_1	0.16	0.119–0.12	0.115	19.6–20.5	20.7	20.9	0.4	0.45
W_{12}	0.31	–	0.112	–	17.7	18.3	0.93	1.02
W_{123}	0.44	0.079–0.11	0.11	9.7–11.5	14.7	15.7	1.5	1.61
W_{1234}	0.54	–	0.109	–	11.9	13.1	1.96	2.08

that the damaged responses of the ropes analyzed in this study are length-independent (illustrated in Fig. 1c with the particular rope W_{12}), except near the ropes ends where axial strain distribution strongly depends on the boundary conditions of the rope. Lastly, the lateral deflection of a rope, whose direction is represented by the arrows in Fig. 1c relative to its initial straight configuration for the rope W_{12}, increases as the degree of asymmetry of the rope cross-section gets bigger as presented in Table 1 for two rope axial (natural) strain (ε) values (0.025 and 0.071). The maximum lateral deflection reported is for rope W_{1234} ($\varepsilon = 0.071$) which value is equal to 2.08 mm, which is about 35% of the rope diameter and the deflection-to-rope length ratio is equal to 0.0035 that can be considered a small perturbation of the initial rope geometry. Although 3D FE simulations predict that the asymmetric damaged distribution to rope cross-section slightly perturb the initial rope geometry, its effect on rope residual strength and rope deformation capacity should be properly considered in order to estimate rope service life at the design stage and to establish the appropriate rope inspection methods and discard criteria as previously commented. Despite 3D FE models provide accurate details and good estimation on asymmetrically damaged rope response, they demand a high computational cost [18]. Hence, the use of simpler and computationally cheaper analytical models that can provide comparable results relative to 3D FE simulations can be more attractive for rope design and performance prediction.

2.2. Proposed analytical model

The description of a proposed simplified mechanical model developed to account for the loss of symmetry of rope cross-section due to the failure of individual rope components is presented hereafter in detail. It is assumed that the response of an asymmetric damaged rope can be accurately predicted by uncoupled biaxial rope responses (i.e., two uniaxial bending analyses). Therefore, the proposed model is based on the equations that govern the response of a nonlinear planar beam considering Bernoulli's kinematic hypothesis (plane sections of a beam remain plane and normal to its centroidal axis after deformation) and assumptions adopted based on the results given by 3D FE simulations previously mentioned. In the following, the proposed model is referred as NLBM (nonlinear beam model).

Consider the geometry of deformation (assuming Bernoulli's kinematic hypothesis) and the equilibrium of a planar (xy plane) rope segment $[x, x + \Delta x]$ as shown in Fig. 2 where $u(x)$ is the displacement of the centroid in the axial direction; $v(x)$ is the displacement of the centroid in the transverse direction; $\lambda(x)$ is the rotation of the normal to the cross-sectional plane (not shown in the figure); $H(x)$ and $V_y(x)$ are the horizontal and vertical forces relative to the axial and transverse direction of the undeformed rope; $M_{zz}(x)$ is the bending moment around z axis; and $h(\xi)$, $q_y(\xi)$, and $m_{zz}(\xi)$ are distributed axial force, transverse force and bending moment respectively along the rope segment.

From the balance of forces in the axial and transverse directions, the moment equilibrium about the point P (Fig. 2), and considering the limit as $\Delta x \to 0$, the following equilibrium equations are obtained [23]

$$\frac{dH}{dx} + h(x) = 0 \tag{1}$$

$$\frac{dV_y}{dx} + q_y(x) = 0 \tag{2}$$

$$\frac{dM_{zz}}{dx} + V_y\left(1 + \frac{du}{dx}\right) - H\frac{dv}{dx} + m_{zz}(x) = 0 \tag{3}$$

Considering that the slopes of the deformed longitudinal axis of the rope (beam) are small compared to unity, small angle approximation assumption is used in this study. Hence, rope curvature can

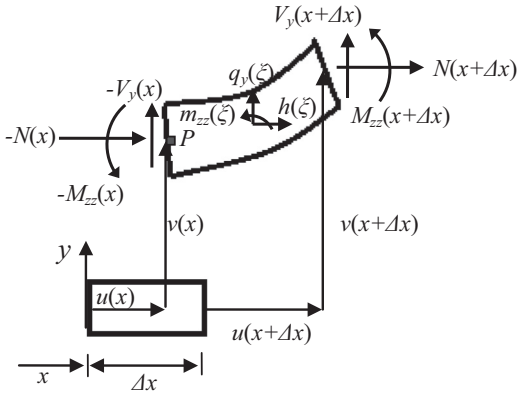

Fig. 2. Equilibrium of a beam segment.

be approximated by the second derivative of the lateral displacement $v(x)$ (respect to the initial rope configuration); and by using the Bernoulli's kinematic hypothesis and the secant formulation to estimate the bending stiffness [24], the moment–curvature relationship for a rope is given by

$$M_{zz} = (EI_{zz})_{\text{sec}} \frac{d^2 v}{dx^2} \tag{4}$$

where $(EI_{zz})_{\text{sec}}$ is the secant bending stiffness of the cable respect to the z-axis. In the above equation, it is assumed that the relative slip among rope components is prevented; thus rope components are bent around the rope neutral axis (i.e., stick state [24]). Combining the first derivative of Eqs. (3) to (2) and (4) along with the fact that axial strain is constant along rope components (Fig. 1), which implies that $d^2u(x)/dx^2 = 0$, and considering the absence of distributed axial force $h(\xi)$ and bending moment $m_{zz}(\xi)$, lead to the following fourth order differential equation

$$(EI_{zz})_{\text{sec}} \frac{d^4 v}{dx^4} - q_y(x)\left(1 + \frac{du(x)}{dx}\right) - H(x)\frac{d^2 v}{dx^2} = 0 \tag{5}$$

Similarly, the differential equation that governs the rope deflection $w(x)$ in the xz plane is given by

$$(EI_{yy})_{\text{sec}} \frac{d^4 w}{dx^4} - q_z(x)\left(1 + \frac{du(x)}{dx}\right) - H(x)\frac{d^2 w}{dx^2} = 0 \tag{6}$$

where $q_z(x)$ is the distributed force along the rope length in the z direction and $(EI_{yy})_{\text{sec}}$ is the secant bending stiffness of the cable respect to the y-axis

The values of the distributed forces $q_y(x)$ and $q_z(x)$ are estimated based on the same assumption established in [15]: radial forces exerted on rope core are not in equilibrium due to the loss of symmetry of the rope cross-section. Hence, considering the helical nature of the rope components that lay in the second layer of the rope, net transverse forces in both xy and xz planes, $q_y(x)$ and $q_z(x)$ respectively, act perpendicular to rope longitudinal (centroidal) axis inducing a lateral deflection in the $-y_1$ direction as shown in Fig. 3, in which y_1 is the axis of symmetry of the damaged rope cross-section. Neglecting the shear forces in rope components, the value of the radial line body force X_2 can be estimated as [25]

$$X_2 = \kappa_2 T_2 \tag{7}$$

where κ_2 and T_2 is the curvature and tensile load of a helical rope component located in layer 2, for a given value of the rope axial strain ε. In order to illustrate the process to compute the aforementioned transverse forces, the particular case of the damaged rope cross-section shown in Fig. 3 is analyzed assuming that the unbroken rope components are mainly in radial contact with the rope

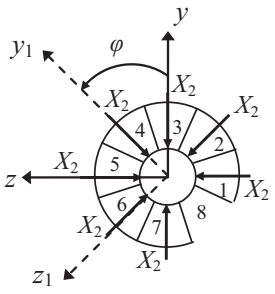

Fig. 3. Radial equilibrium in an asymmetric damaged rope cross-section.

core. The radial line body force rope component 4 is unbalanced due to the failure of rope component 8 (Fig. 3). Hence, the net line transverse forces along the longitudinal axis of the rope in both xy and xz planes are given by

$$q_y = \frac{-\kappa_2 T_2 \cos\varphi}{\cos\theta_2} \tag{8a}$$

$$q_z = \frac{-\kappa_2 T_2 \sin\varphi}{\cos\theta_2} \tag{8b}$$

where φ is the swept angle of the rope components and θ_2 is the helix angle of the rope components of the second layer. Thus, for any type of asymmetric damage distribution to rope cross-section, the net transverse forces $q_y(x)$ and $q_z(x)$ can be expressed as:

$$q_y = -K(\varepsilon)\cos\varphi \tag{8c}$$

$$q_z = -K(\varepsilon)\sin\varphi \tag{8d}$$

where de function $K(\varepsilon)$ captures the unbalanced transverse force in the y_1 direction as already illustrated in Eqs (8a) and (8b) projected on the longitudinal axis of the rope [16]. In order to capture the dependence of the z_1y_1 plane (Fig. 3) on the helical nature of rope components in the initial rope configuration, the swept angle φ is related to the position along the rope longitudinal axis x throughout the relationship $\varphi = (2\pi x/p)$, where p is the pitch distance of rope components. As such, the damaged rope is analyzed with a constant cross-section in which the axes zy and z_1y_1 (principal axes of the cross-section) coincide and the helical nature of rope components in the initial rope configuration is captured by the net transverse forces $q_y(x)$ and $q_z(x)$.

The boundary conditions specified to the rope model are similar to the ones defined in the 3D FE models [18] and during the ropes tests [10] which are depicted in Fig. 4, where the notation $(\cdot)' = d(\cdot)/dx$ is used for the first derivate:

- Section A ($x = 0$) of the rope is fully clamped: $v_{x=0} = 0$; $w_{x=0} = 0$; $v'_{x=0} = 0$; and $w'_{x=0} = 0$.
- At section B ($x = L$) an axial displacement history is specified ($u_{x=L} = \Delta u$) where L is the updated rope length; and the cross-section is prevented from rotating and laterally deflecting: $v_{x=L} = 0$; $w_{x=L} = 0$; $v'_{x=L} = 0$; and $w'_{x=L} = 0$.

The Eqs. (5) and (6) have closed-form solutions for a given value of rope axial strain ε, considering the general expressions for the forces $q_y(x)$ and $q_z(x)$ given in Eqs. (8c) and (8d) respectively. The general solution for $v(x)$ and $w(x)$ are given by

$$v(x) = \frac{a_z}{b_z c^2 + c^4}\cos(cx) + C_1\frac{e^{\sqrt{b_z}x}}{b_z} + C_2\frac{e^{-\sqrt{b_z}x}}{b_z} + C_4 x + C_3 \tag{9}$$

$$w(x) = \frac{a_y}{b_y c^2 + c^4}\sin(cx) + C_5\frac{e^{\sqrt{b_y}x}}{b_y} + C_6\frac{e^{-\sqrt{b_y}x}}{b_y} + C_8 x + C_7 \tag{10}$$

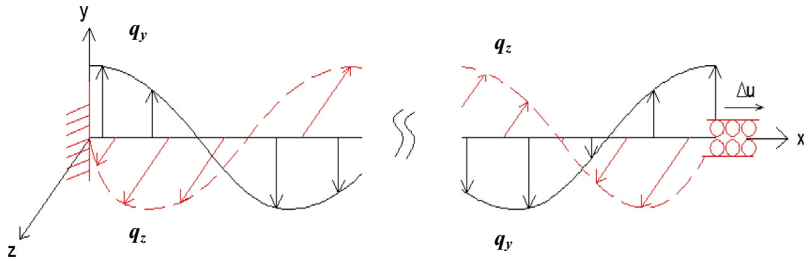

Fig. 4. Sketch of the loads and boundary conditions of the model.

where $a_z(\varepsilon) = -K(\varepsilon)(1 + \Delta u/L)/(EI_{zz})_{sec}$; $a_y(\varepsilon) = -K(\varepsilon)(1 + \Delta u/L)/(EI_{yy})_{sec}$; $b_z(\varepsilon) = H(\varepsilon)/(EI_{zz})_{sec}$; $b_y(\varepsilon) = H(\varepsilon)/(EI_{yy})_{sec}$; and $c = 2\pi/p$. Accounting for the boundary conditions previously specified, the expressions for the parameters C_i ($i = 1, \ldots, 8$) are

$$C_1 = 0; \quad C_2 = 0; C_4 = 0; \quad C_3 = -\frac{a_z}{b_z c^2 + c^4} \tag{11a}$$

$$C_5 = -\frac{La_y b_y e^{-L\sqrt{b_y}}}{c(c^2 + b_y)\left(2e^{-L\sqrt{b_y}} + L\sqrt{b_y} + L\sqrt{b_y}e^{-L\sqrt{b_y}} - 2\right)} \tag{11b}$$

$$C_6 = -\frac{La_y b_y}{c(c^2 + b_y)\left(2e^{-L\sqrt{b_y}} + L\sqrt{b_y} + L\sqrt{b_y}e^{-L\sqrt{b_y}} - 2\right)} \tag{11c}$$

$$C_7 = -\frac{La_y(e^{-L\sqrt{b_y}} - 1)}{c(c^2 + b_y)\left(2e^{-L\sqrt{b_y}} + L\sqrt{b_y} + L\sqrt{b_y}e^{-L\sqrt{b_y}} - 2\right)} \tag{11d}$$

$$C_8 = -\frac{2a_y(e^{-L\sqrt{b_y}} - 1)}{c(c^2 + b_y)\left(2e^{-L\sqrt{b_y}} + L\sqrt{b_y} + L\sqrt{b_y}e^{-L\sqrt{b_y}} - 2\right)} \tag{11e}$$

Based on the Bernoulli's kinematics hypothesis, the assumption of small lateral displacements, small strains, and small rotations for each iterative procedure at each step of the proposed numerical algorithm later explained; and the expressions for the transverses displacements $v(x)$ and $w(x)$ given by Eqs. (9) and (10) respectively, the displacement field of a generic point at section x can be referred to the displacements $u(x)$, $v(x)$ and $w(x)$ of the centroid at same section as follows

$$u_x(x) = u(x) - y\frac{dv(x)}{dx} + z\frac{dw(x)}{dx} \tag{12a}$$

$$u_y(x) = v(x) \tag{12b}$$

$$u_z(x) = w(x) \tag{12c}$$

where $u_x(x)$, $u_y(x)$, and $u_z(x)$ denote the displacements in the x, y, and z directions respectively (Fig. 3) of the generic point ((z,y) location at rope cross-section) under consideration. In this formulation, the effect of the angle of twist of the cable on its lateral deflections $v(x)$ and $w(x)$ is neglected. Consequently, the axial strain ε_t of the generic point is estimated as

$$\varepsilon_t(x) = \frac{du_x(x)}{dx} \tag{13}$$

As previously stated, the particular application of the proposed model presented in this study is focused on PET asymmetrically damaged ropes. The nonlinear constitutive response of the rope components is directly obtained from the experimental data reported in [10]. As such, the degradation of the mechanical properties of the PET rope components experienced when they are subjected to stretching is properly accounted for [26]. A polynomial function up to the fifth degree is used to express the normal stress σ_t of a generic point as a function of its normal strain ε_t, having the following form

$$\sigma_t(\varepsilon_t) = \sigma_{t\max}\left[\sum_{k=1}^{5}\gamma_k\left(\frac{\varepsilon_t}{\varepsilon_{t\max}}\right)^k\right] \tag{14}$$

where the coefficients γ_k are constitutive parameters that are chosen to provide a best fit to measured data for rope components; and σ_{tmax} (897 MPa) and ε_{tmax} (0.117; natural strain) are the maximum stress and strain at the onset of rope component failure respectively.

In the following an iterative cross-sectional displacement control algorithm developed based on the solutions of Eqs. (5) and (6) to asses the capacity curves of asymmetrically damaged ropes is presented for each increment of the rope axial displacement, in which the unbroken rope components are assumed to behave as fiber elements (i.e., they only develop uniaxial state of stress). This algorithm proceeds with the following steps for the jth incremental step of the analysis:

Step 1: Given a rope axial displacement increment value Δu_j, an initial horizontal force value H_j^i ($i = 0$), considering the initial helical geometry of the rope components (i.e., straight rope) and their individual contribution to rope axial load (discrete formulation), is estimated as follows

$$u_j = u_{j-1} + \Delta u_j \tag{15a}$$

$$H_j^i = \sum_k A_k\sigma_k\left(\frac{u_j}{L_0}\cos^2(\theta_0)_k\right)\cos(\theta_0)_k \tag{15b}$$

where u_j is the total rope axial displacement in the jth incremental step of the analysis; σ_k is the normal stress as a function of the axial strain computed from Eq. (14) considering the centroid of the kth unbroken rope component as the generic point t and A_k is the cross-sectional area of the kth unbroken rope component. For simplicity, in the above equation, the linearized strain–displacement equation for rope components is utilized [27].

Step 2: Compute the net transverse forces $(q_y)_j^i(x, \varepsilon_j)$ and $(q_z)_j^i(x, \varepsilon_j)$ through Eqs. (8c) and (8d) respectively, considering the corresponding cross-section damage distribution to evaluate the function $K_j^i(\varepsilon_j)$ also considering the initial helical geometry of the rope components.

Step 3: Determine the lateral deflections (i.e. the updated rope configuration ($i \to i + 1$)) $v(x)_j^{i+1}$ and $w(x)_j^{i+1}$ through Eqs. (9)–(11e) for the total rope axial displacement given in the jth incremental step of the analysis u_j (Eq. (15a)). To this end, use an initial average secant modulus $(E_{sec})_0$ ($i = 0$) defined as

$$(E_{sec})_0 = \frac{\sum_k\left[(AE(\varepsilon_{k0}))_k\right]}{\sum_k A_k} \tag{16}$$

where subscript k accounts for the unbroken rope components and ε_{k0} is the axial strain of the kth unbroken rope component for an arbitrary small rope axial strain value computed considering straight rope configuration.

Step 4: The displacement field $u_{xk}(x)_j^{i+1}$, $v_k(x)_j^{i+1}$ and $w_k(x)_j^{i+1}$ is computed for the kth unbroken rope component through Eq. (12) considering the centroid of each unbroken rope component as the generic point (coordinates (z_k, y_k)). Based on this displacement field, the curvature of each unbroken rope component can be calculated in its deformed configuration. Let $(\xi_k)_j^{i+1} = (u_{xk}(x)_j^{i+1},\ v_k(x)_j^{i+1},\ w_k(x)_j^{i+1})$ be the updated $(i \to i+1)$ position vector of the kth unbroken rope component; hence its updated curvature is given by [28]

$$(\kappa_k)_j^{i+1} = \frac{\left[((\xi_k)_j^{i+1}\cdot(\xi_k)_j^{\prime i+1})((\xi_k)_j^{\prime i+1}\cdot(\xi_k)_j^{\prime i+1}) - ((\xi_k)_j^{i+1}\cdot(\xi_k)_j^{\prime i+1})^2\right]^{1/2}}{((\xi_k)_j^{i+1}\cdot(\xi_k)_j^{i+1})^{3/2}} \tag{17}$$

where $(\cdot)' = d^2(\cdot)/dx^2$ is used for the second derivate.

Step 5: Compute the axial strain value $(\varepsilon_k)_j^{i+1}$ for the kth unbroken rope component also considering its centroid as the generic point using Eq. (13). The expression for $u_x(x)$ $(u_{xk}(x)_j^{i+1})$ given by Eq. (12a) is multiplied by the factor $\cos^2\theta_k$ to account the helical shape of the kth unbroken rope component. This factor assumes, based on the results given by 3D FE models, that the deformed configuration of the unbroken rope components obtained from Eqs. (9) and (10) is close to a circular helix as shown in Fig. 5. In this figure, for a wide range of IA values (W_{136}, W_1, W_{123}, and W_{1234} ropes), it is shown that ropes curvatures in their deformed configurations computed from adjusted first order circular helix curves match quite well (ratios values close to 1) with the curvatures obtained from Eq. (17), in which the normalized curvatures for each rope are represented in the horizontal axis. For computational purposes, it is assumed that the lateral deflection of the rope induces a helix radius change of each rope component as proposed in [15]. As such, the value the updated value of the helix angle θ_k is obtained from the expression $\tan(\theta_k)_j^{i+1} = 2\pi(R_{hk})_j^{i+1}/p(\varepsilon_j)$, where $(R_{hk})_j^{i+1}$ is the equivalent helix radius of the kth unbroken rope component in its deformed configuration for the iteration $(i+1)$ (distance from the centroid of the rope core to the centroid of the rope component) and $p(\varepsilon_j)$ is the updated pitch distance related to the rope axial strain ε_j at the jth incremental step of the analysis.

Step 6: The normal stress for the kth unbroken rope component $(\sigma_k)_j^{i+1}$ is calculated using Eq. (14) considering its centroid as the generic point. It is assumed that the normal stress is distributed uniformly throughout rope component cross-section; thus, the axial force developed by the kth unbroken rope component is given by $(T_k)_j^{i+1} = A_k(\sigma_k)_j^{i+1}$.

Step 7: Compute the updated horizontal force value H_j^{i+1} $(i \to i+1)$ as follows

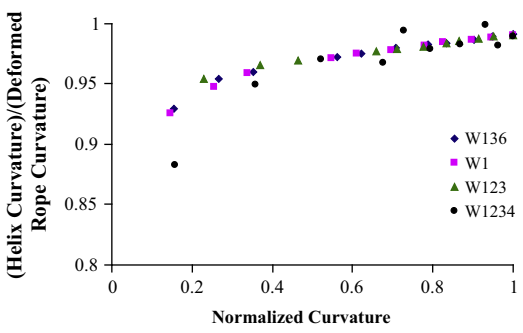

Fig. 5. Curvature of deformed rope configurations versus helical shape curvature.

$$H_j^{i+1} = \left[\sum_k (T_k)_j^{i+1}\cos(\theta_k)_j^{i+1}\right] \tag{18}$$

Step 8: Compute the error value of the horizontal force $(errH)_j^{i+1}$ as

$$(errH)_j^{i+1} = \frac{|H_j^{i+1} - H_j^i|}{H_j^i} \tag{19}$$

where $|\ |$ is the modulus function. If the value of $(errH)_j^{i+1}$ is less than a prescribed tolerance (5E-4 used in this study) the horizontal force value for the jth increment in axial displacement Δu_j is H_j^{i+1}, and a new analysis is performed for the $(j+1)$th increment in axial displacement Δu_{j+1}. If not, compute an average secant modulus $(E_{sec})_j^{i+1}$ and repeat from *Step 2* to *Step 8* considering the updated values of the deformation geometry of the unbroken rope components. The expression to compute $(E_{sec})_j^{i+1}$ is given by

$$(E_{\text{sec}})_j^{i+1} = \frac{\sum_k [(AE(\varepsilon_k))_k]_j^{i+1}}{\sum_k A_k} \tag{20}$$

which is a necessary value to solve the Eqs. (5) and (6) accounting for the rope deformed configuration in the $(i+1)$ iteration during the jth analysis step.

3. Numerical examples and discussion

The validation of the proposed model is presented in a concise manner. To this end, comparisons between rope axial load and rope axial strain curves obtained from 3D FE simulations, NLBM (proposed model), two linear models reported in the literature [13,15] and experimental data [10] are shown in Fig. 6 for three (W_{136}, W_1, and W_{123}) of the five ropes analyzed in this study. The linearity of the aforementioned analytical models is meant to the linearization of the strain–displacement equation for rope components and the assumption of linear deflection theory (axial loads and transverse deflections are uncoupled). Damaged cross-sections have been incorporated to the plots as a reference in which broken rope components are colored gray.

Predicted curves obtained from Lanteigne (Appendix B) and MacDougall and Bartlett (M-B) (Appendix C) linear models for ropes W_{136} and W_1 are almost identical and consequently they show similar behavior when compared with 3D FE simulations curves: good correlation of the rope tangent stiffness but they underestimate both rope residual strength and rope axial failure strain in about 10%. Experimental data curves of rope W_1 are slightly softener than the aforementioned predicted curves in which the underestimation of rope residual strength and rope axial failure strain increases to 15%. For the case of experimental curves of rope W_{136}, two of them (Exp. data 2 and Exp. data 3 curves) failed earlier and Exp. data 1 curve is stiffer than all the predicted curves and the associated measured residual strength and rope axial failure strain values are overestimated by the Lanteigne and M-B models in 17% and 8% respectively. These two linear analytical models do not provide satisfactory results for greater degree of asymmetry of the type of damaged rope cross-sections considered in this study ($IA > 0.16$, value for W_1 rope) due to the large curvatures and large lateral deflection of the ropes estimated. In these cases, asymmetric damaged ropes responses became considerable more flexible than 3D FE and experimental curves because opposite unbroken rope components to damage develop compression stresses [29] as discussed later in the paper (Fig. 10).

For the case of the predicted curves obtained from the NLBM, they are slightly stiffer than the curves predicted by Lanteigne, M-B and 3D FE models comparing quite well with Exp. data 1 curves for both W_{136} ($IA = 0.09$) and W_{123} ($IA = 0.44$), although

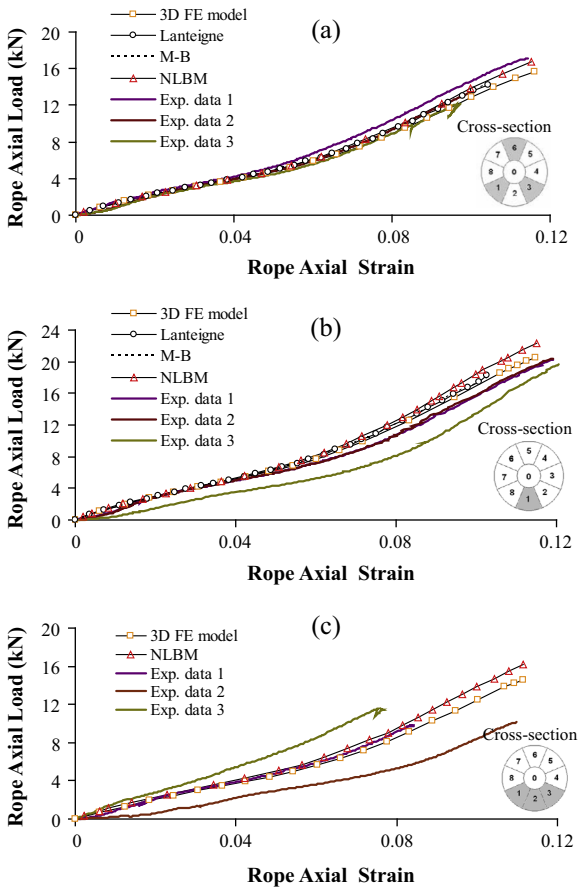

Fig. 6. Capacity curves of asymmetric damaged ropes: (a) W_{136}; (b) W_1; and (c) W_{123}.

the latter fails earlier probably due to a progressive damage of rope components around rope terminations as reported by the researcher who conducted the tests [10]. The other two experimental curves of rope W_{123} (Exp. data 2 and exp. data 3) bound the predicted responses (3D FEM and NLBM curves), but reaching smaller axial failure strain values probably for the same reason previously mentioned. Two experimental curves (Exp. data 1 and Exp. data 2) of rope W_1 and NLBM curve match very close up to a rope axial strain value equal to 0.06; for greater strain values, these curves start diverging being the NLBM curve an upper bound for experimental curves. Contrary to the results given by the Lanteigne and M-B models, NLBM simulations provide better estimates for a broader degree of asymmetry values (*IA* values) when compared to the results extracted from a traditional and well accepted 3D FE approach. In Tables 2 and 3, a summary of the residual ropes strengths and failure axial strains is provided for *IA* values that range from 0.09 (W_{136} rope) to 0.54 (W_{1234} rope) respectively, including the values associated to the intact rope (W_u). The NLBM simulations overestimate in a range of [8%, 12%] the residual strength, in which the lower bound is related to the comparison of the W_{136} rope and the upper bound to the W_{1234} rope; and overestimate as well in less than 2% the failure axial strain relative to 3D FE models results. If the net area effect model is used to estimate the residual strength value of a particular damaged rope, the contribution to rope response of the broken rope components is just neglected and the intact rope response curve is multiplied by the parameter ρ_A that represents the remaining cross-sectional area of the rope. In the following paragraphs, the relationship between the variation of the residual rope strength and failure axial strain values provided by the numerical and analytical models and the parameter ρ_A is analyzed in detail.

In order to establish the dependency of the residual strengths predicted by the analytical and numerical models considered in this study on the remaining cross-sectional area of the damaged ropes, two net area effect curves are included in Fig. 7a. Net area 1 curve considers the intact rope response curve given by the 3D FE model and the Net area 2 curve the intact rope response curve provided by a model based on the linearized strain–displacement equation for rope components that assumes that rope components only develop tensile load [24]. This distinction is necessary due to the fact that, as already stated, the analytical models (Lanteigne, M-B, and NLBM) rely on the linearization of the strain–displacement equation and uniaxial rope components behavior, neglecting friction forces and local contact deformations (assumption validated in [26]); forces and deformations considered by the 3D FE model formulation [18]. As a result, predicted intact rope strength given by the 3D FE model is overestimated in about 6% by the linearized model as shown in Fig. 7a for a value of ρ_A equal to 1. 3D FE model and NLBM curves have similar behavior when comparing with their corresponding net area effect curves: they slightly deviate (residual strength values decrease almost linearly with the rope cross-sections) from their corresponding net area effect curves (Net area 1 for 3D FE curve and Net area 2 for NLBM curve), presenting a discontinuity at $\rho_A = 0.66$ due to the fact that ropes W_{136} and W_{123} have the same number of broken components but differing in their distribution throughout rope cross-section leading to a greater *IA* value for rope W_{123} (0.44) than for rope W_{136} (0.092) which results in an additional relative reduction of the rope residual strength of 6% and 4% for the 3D FE model and NLBM respectively. Thus, for both models their corresponding net area effect curves accurately estimate the residual strength of ropes with *IA* values less than 0.44 and also both models capture the dependency of the residual strength value on the degree of asymmetry of the cross-section. For *IA* values greater than 0.44, both models slightly increase their deviation with respect to their corresponding net area effect curves reaching values equal to 10% and 5% for the 3D FE model and NLBM respectively, for rope W_{1234} ($IA = 0.54$). Conversely, Lanteigne and M-B curves substantially deviate from their net area effect curve (Net area 2) for the entire range of *IA* values considered for these two models ([0.092–0.31]) except for rope W_{136} ($IA = 0.092$) whose deviation value reached is close to 15%. As a reference, experimental data are also plotted in this figure [10]. Their average values deviate from the net area effect curve (Net area 1) in less than 10% for values of $IA \leqslant 0.16$ (ropes W_{136} and W_1). Conversely, for rope W_{123} ($IA = 0.44$) average reduction in rope strength deviate from linearity significantly reaching values close to 30% [18]. As previously stated, however, researcher who conducted the tests reported that some of these specimens fail earlier near ropes terminations [10].

In Fig. 7b the dependency of the rope failure axial strain as a function of the degree of asymmetry (*IA* value) of the rope cross-section is presented. In general, the predicted values given by the 3D FE, NLBM, Lanteigne, and M-B models have a similar trend: as the value of *IA* increases, the value of the rope failure strain decreases. The values predicted by the NLBM match quite well (difference is less than 2%) with the values given by the 3D FE models for the entire range of index of asymmetry (*IA*) considered ([0.092–0.54]). For a large *IA* value (i.e., 0.54 for rope W_{1234}) the reduction of the rope failure strain relative to the intact case (0.117) is 7%. On the other hand, values predicted by the Lanteigne, and M-B models compare quite well between each other, but they underestimate in about 10% the values predicted by the 3D FE models that are used as references as previously discussed. Comparisons between experimental data and the predicted values given by the 3D FE model were extensively discussed in reference [18], but they are

Table 2
Summary of the rope residual strength values for asymmetric damaged ropes.

Rope	$(IA)_0$	Exp. data	3D FE model	Lanteigne model	M-B model	NLBM
W_u	0	22.3–25.6	23.5	24.9	25	25
W_{136}	0.093	12.2–17	15.6	14.3	14.2	16.8
W_1	0.16	19.6–20.5	20.7	18.2	18.2	22.3
W_{12}	0.31	–	17.7	13.0	12	19.4
W_{123}	0.44	9.7–11.5	14.7	–	–	16.2
W_{1234}	0.54	–	11.9	–	–	13.3

Table 3
Summary of the failure of the failure axial strain values at the onset of failure for asymmetric damaged ropes.

Rope	$(IA)_0$	Exp. data	3D FE model	Lanteigne model	M-B model	NLBM
W_u	0	0.115–0.127	0.117	0.117	0.117	0.117
W_{136}	0.093	0.097–0.114	0.115	0.104	0.104	0.115
W_1	0.16	0.119–0.12	0.115	0.104	0.104	0.115
W_{12}	0.31	–	0.112	0.1	0.097	0.114
W_{123}	0.44	0.079–0.11	0.11	–	–	0.111
W_{1234}	0.54	–	0.109	–	–	0.11

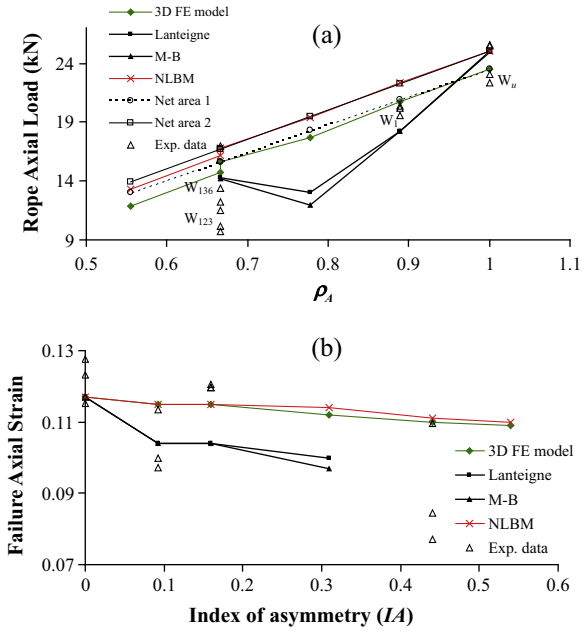

Fig. 7. Dependency analysis: (a) residual strength on remaining cross-sectional area (ρ_A); (b) failure strain on index of asymmetry (IA).

also included in this figure for completeness. The measured values are well predicted by both 3D FE and NLBM models for values of IA less than 0.16 (ropes W_{136} and W_1) within a range of −4% to +13%. For values of IA greater than 0.16 (rope W_{123}), average measured value is overestimated by the numerical and analytical models in 25%. It is important to point out, however, that in reference [18] was mentioned that some difficulties experienced during rope testing (rope load was unevenly distributed in rope terminations resulting in premature rope failure [10]) as the IA value increased that may explain the variability of the results and the difference between predicted and measured values for some of the ropes tested.

The stress distributions throughout asymmetric damaged rope cross-section predicted by the numerical and analytical models are compared from Figs. 8–10, in which three ropes are selected to carry out these comparative analyses: W_{136}, W_1, and W_{12}. Comparisons are intended to establish the validity of the analytical models (Lanteigne, M-B, and NLBM) when compared with the results given by the 3D FE models considered as reference. As in the case of the computation of the displacement field of the unbroken rope components (*Step 4* of the numerical algorithm), the centroid of these components is considered as the generic (representative) point to compute their tensile stress estimated by the analytical models. Conversely, as the 3D FE models predict a gradual variation in the strain/stress distribution throughout unbroken rope components cross-sections as commented in Fig. 1, the maximum and minimum values are plotted for comparison purposes and also to define a range of values that allow determining the accuracy of the estimated values given by the analytical models (hereafter referred as admissible values).

Based on Figs. 8–10, tensile stress distribution throughout asymmetric damaged rope cross-section predicted by all models has the same pattern (analysis also valid for the axial strain distribution): closer components to damage are more stressed than the components on the opposite side. This gradient in the stress distribution can be attributed to the lateral deflection of the rope that induces additional bending stresses in the rope components, conclusion that is supported with the discussion provided in the following paragraphs. For notation purposes, the unbroken components numbered m and n of the rope W_{ij} are cited in the text as $W_{ij,mn}$. Lanteigne and M-B models predict comparable tensile stress values for the unbroken rope components of the selected ropes, except for the components $W_{12,56}$ (Fig. 10) in which the Lanteigne model gives considerable higher values. Both models have similar tendency when compared with the values given by the 3D FE models: overestimate tensile stress values of rope components that are adjacent to damage in about 20%; predicted tensile stress values of rope components close to the rope centroid are within the range values defined by the 3D FE simulations; and underestimate stress values of the components that are on the opposite side to damage in about 20% for component $W_{1,5}$ ($IA = 0.16$ for rope W_1) and 15% and over 100% for components $W_{12,82}$ and $W_{12,65}$ ($IA = 0.31$ for rope W_{12}), respectively. Thus, the stress gradient throughout damaged rope cross-section estimated by these two models is higher than the gradient estimated by the 3D FE models and as the IA rope value increases, the underestimation of the tensile stress of the components on the opposite side to damage increases as well. In fact, for ropes with greater IA values (W_{123}, W_{1234}), rope components on the opposite side to damage start developing compressive load resulting in a more flexible damaged rope response relative to 3D FE and NLBM simulations as previously commented. Based upon their formulations, Lanteigne and M-B models do not account for the nonlinearity in equations of equilibrium (effect of axial load on flexural behavior of the rope in this case); thus large lateral deflections are predicted leading to high compressive load due to bending.

Conversely to the results provided by Lanteigne and M-B models previously discussed, the unbroken components tensile stress values provided by the NLBM lay in the ranges of the admissible values defined the 3D FE models for all the ropes presented in this figure (IA values $\in [0.093, 0.31]$), matching quite well with the upper values of the aforementioned ranges for the entire range of the rope axial strain values as already discussed in Fig. 6 (capacity curves). It is important to point out, that additional numerical simulations, not shown here to avoid repeated and extensive analyses, have carried out for ropes W_{123} ($IA = 0.44$) and W_{1234} ($IA = 0.54$) in which the same previous comparison pattern between the unbroken rope component tensile stress values given by the 3D FE and NLBM models is found [29].

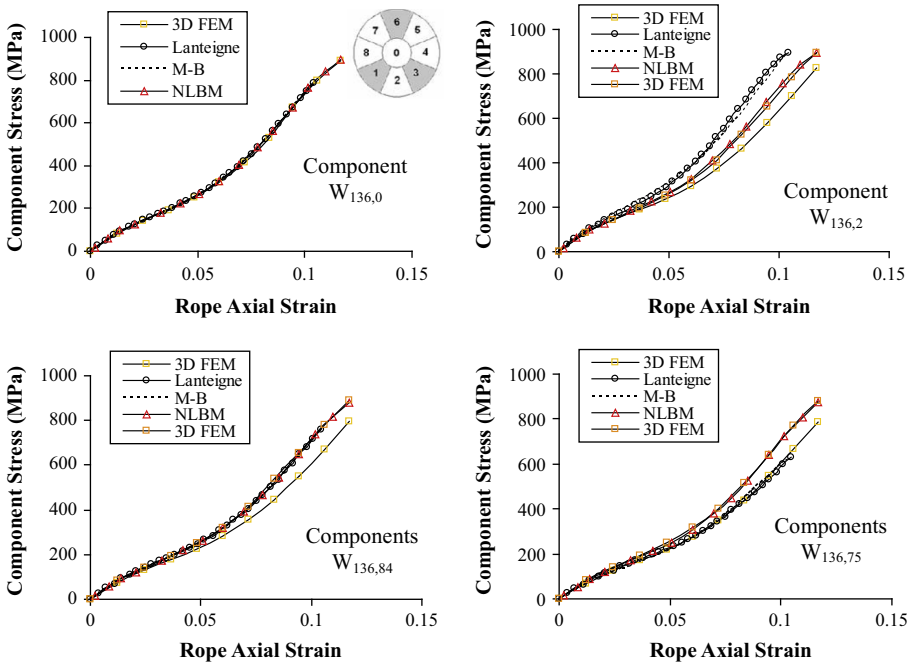

Fig. 8. Tensile stress values of the unbroken components of rope W_{136}.

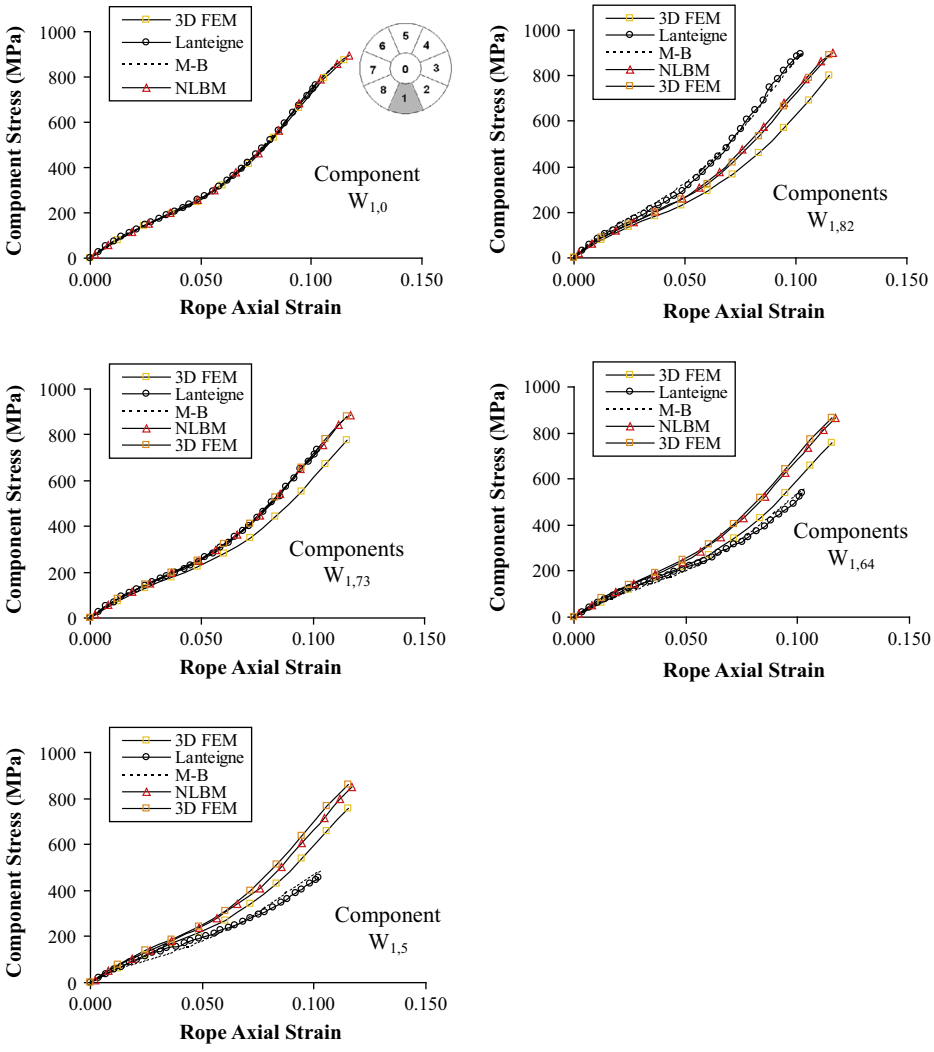

Fig. 9. Tensile stress values of the unbroken components of rope W_1.

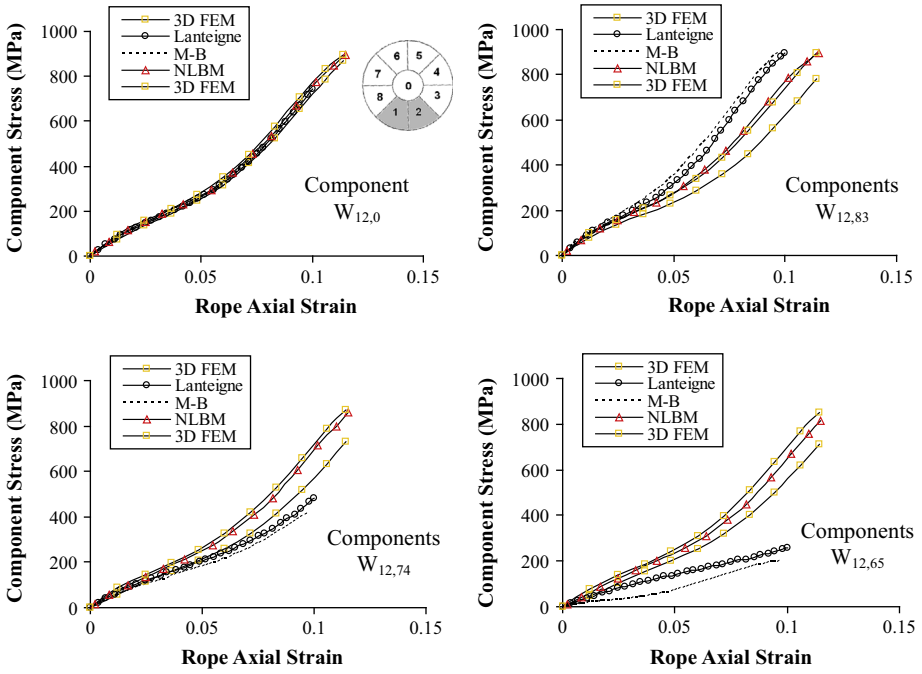

Fig. 10. Tensile stress values of the unbroken components of rope W_{12}.

In Fig. 11 comparisons of the deformed configuration of the ropes W_{136} and W_1 estimated by the 3D FE, NLBM, and M-B models are presented for two rope axial strain values (ε = 0.031 and 0.071). The deformed configuration of an asymmetrically damaged rope estimated by the proposed model (NLBM) is based on the solutions of the governing equations given by the Eqs. (9) and (10) and for the case of the M-B model is given by Eq. (C1) (Appendix C). These two ropes were selected for comparisons purposes because the three aforementioned models give similar results in terms of the capacity curves and stress (strain) distributions throughout rope cross-sections according to the analyses already presented. The deformed configurations of both ropes given by the M-B model are plotted only around the failure region (ropes midspans) because Eq. (C1) does not account for rope boundary conditions. These estimates largely overestimate the ones predicted by the 3D FE models, in which the overestimation of the maximum lateral deflection value is about 300% for ropes W_{136} and W_1. Conversely, deflected ropes shapes and values (computed by the summation of the deflections in both *xy* and *xz* planes) predicted by NLBM are comparable to the values predicted by the 3D FE simulations. In fact, based upon the results summarized in Table 4 for a wide rope axial strain range (from 0.012 to 0.106), NLBM model underestimates rope lateral deflection values for low level of rope axial strain values (0.024 as an upper limit) for most of the ropes analyzed except for rope W_{1234}, whose deflected shape is, in general, overestimated by the NLBM model. For greater rope axial strain values, the ropes deformed configurations start getting overestimated by the results provided by the NLBM model, but significantly less than those estimated by the M-B model. If the ratio of the values given by both 3D FE and NLBM models are computed for the entire range of rope axial strain earlier specified, it turns out that in an average sense the maximum ropes lateral deflections values are overestimated in the range [12%, 20%] for all the ropes analyzed (W_{136}, W_1, W_{12}, W_{123}, and W_{1234}), in which the values of the central thirds of the ropes are considered to avoid ropes ends effects especially for ropes with low *IA* values, as explained later in the paper. For rope axial strain values close to ropes failures (see Table 2), however, the deflected shape values can be overestimated up to 35% of the references values (3D FE simulations).

Based on the values reported in Table 4, values given by both 3D FE and NLBM models have the same trend: as the *IA* rope value increases (ropes are arranged in increasing order of their *IA* values in Table 4), the rope lateral deflection increases as well. This conclusion suggests that the effect on the lateral displacements in planes *xy* and *xz*, according to Eqs. (9) and (10) respectively, of larger $H(\varepsilon)$ (rope axial force) values (W_{136} values relative to W_1 and W_{12} values) does not compensate the increment of the function $K(\varepsilon)$ with increasing values of *IA*, which determines the net transverse forces $q_y(x)$ and $q_z(x)$ acting on rope cross-section defined in Eqs. (8c) and (8d) respectively. On the other hand, for a particular asymmetric damaged rope (fixed *IA*, I_{zz}, and I_{yy} values), as the value of the axial rope strain (ε) increases, the magnitude of the function $K(\varepsilon)$ increases more rapidly than the magnitude of $H(\varepsilon)$ and consequently, larger lateral displacements are developed by the rope (see expressions for $a_z(\varepsilon)$, $a_y(\varepsilon)$, $b_z(\varepsilon)$, and $a_z(\varepsilon)$ in Eqs. (9) and (10)). When comparing the deflection ropes values estimated by the NLBM and the 3D FE simulations, it is important to emphasize that the magnitude of the lateral deflections predicted by the NLBM model is proportional to the value of the function $K(\varepsilon)$ represented by the parameters $a_z(\varepsilon)$, $a_y(\varepsilon)$, in Eqs. (9) and (10) respectively. For simplicity, the values of the function $K(\varepsilon)$ are computed assuming only radial contact between rope components as previously stated (Eqs. (7)–(8d)). Smaller values of this function, and consequently smaller values of the lateral deflections of the ropes comparable to the ones given by the 3D FE models, would be computed if contact between rope components were defined in both radial and circumferential directions as considered in the 3D FE simulations ([18]).

Despite of the moderate overestimation of the values of the deformed configurations of the ropes previously discussed and unlike the results given by the M-B model, the shape of the deformed configuration of an asymmetric damaged rope is accurately predicted by the NLBM model that accounts for the rope boundary conditions (Fig. 11). The rope deforms laterally describing a curve similar to a circular helix, as discussed in *Step 5* of the numerical algorithm proposed, in which the original longitudinal axis of the rope is shifted in the direction of the damage. In fact, away from the rope ends, in the *xy* plane, the rope describes a

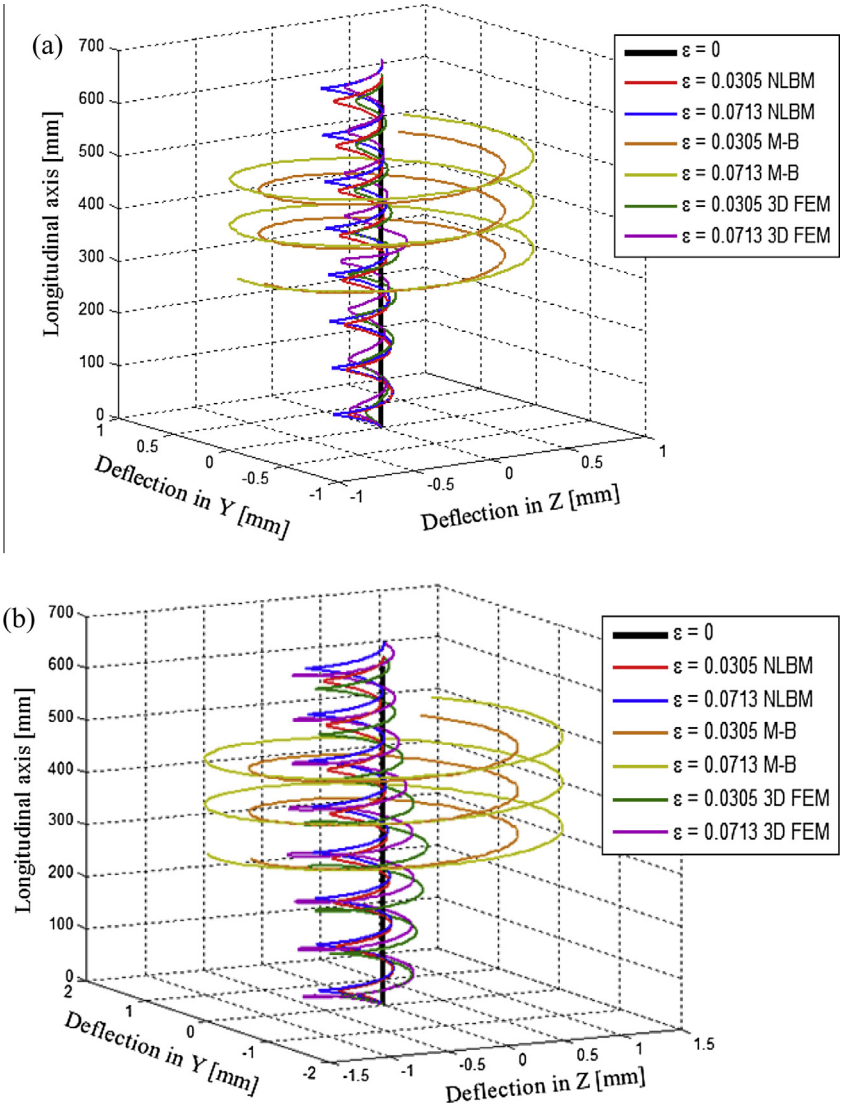

Fig. 11. Deformed configuration of ropes: (a) W_{136} and (b) W_1.

Table 4
Ropes maximum lateral deflections given by 3D FE and NLBM models.

Rope strain	3D FE models					NLBM model				
	W_{136}	W_1	W_{12}	W_{123}	W_{1234}	W_{136}	W_1	W_{12}	W_{123}	W_{1234}
0.012	0.21	0.33	0.78	1.25	1.60	0.17	0.29	0.70	1.20	1.64
0.024	0.24	0.42	0.96	1.51	1.96	0.21	0.38	0.86	1.42	1.90
0.048	0.25	0.45	1.02	1.61	2.08	0.28	0.49	1.08	1.72	2.24
0.072	0.26	0.45	1.03	1.61	2.09	0.32	0.57	1.21	1.92	2.46
0.095	0.27	0.46	1.04	1.63	2.10	0.35	0.63	1.33	2.10	2.68
0.106	0.28	0.47	1.06	1.65	2.12	0.37	0.67	1.41	2.22	2.83

projection of a circular helical curve around a longitudinal axis parallel to the reference (undeformed) one whereas in the *xz* plane the rope also describes a projection of a circular helical curve but around an inclined longitudinal axis relative to the reference one due to the presence of the no null exponential and linear terms in Eq. (10). This characteristic of the deformed configuration of an asymmetric damaged rope is depicted in Fig. 12 for ropes W_{136} and W_{1234}. Based on the 3D FE simulations results, boundary conditions play a crucial role in rope deformed configuration for ropes with low *IA* values. In Fig. 12(a and b), for example, the peaks of the projected helix curves (i.e. helix radius) in *xy* and *xz* planes that represent the deformed configuration of rope W_{136} (*IA* = 0.091, least *IA* value considered in this study) decrease as approaching to the rope ends, phenomena that is not captured by the NLBM model that predicts curves with constant amplitudes as rope deformed configuration in both planes. As the *IA* rope value increases, the boundary conditions effect on rope deformed configuration is only localized in rope sections located at $x = 0$, and $x = L$ (updated rope length) owing to 3D FE simulations estimate helix curves with constant amplitudes (similar to NLBM model) as rope deformed configuration as shown in Fig. 12(c and d) for rope W_{1234} with *IA* value equal to 0.54 (maximum value considered in this study). More details in the evolution of the impact of boundary conditions on rope deformed configuration as the *IA* rope value increases can be found in [29].

Consequently, in terms of the geometry of deformation of the ropes and based on the results given by both 3D FE and NLBM models, the asymmetry in damage distribution to rope cross-section induces a small perturbation of the original first order circular helical geometry of the rope components in which the rope components of the second layer and the core developed approximately a second and first order circular helix curve respectively. The maximum lateral deflection-to-rope initial length ratio (perturbation

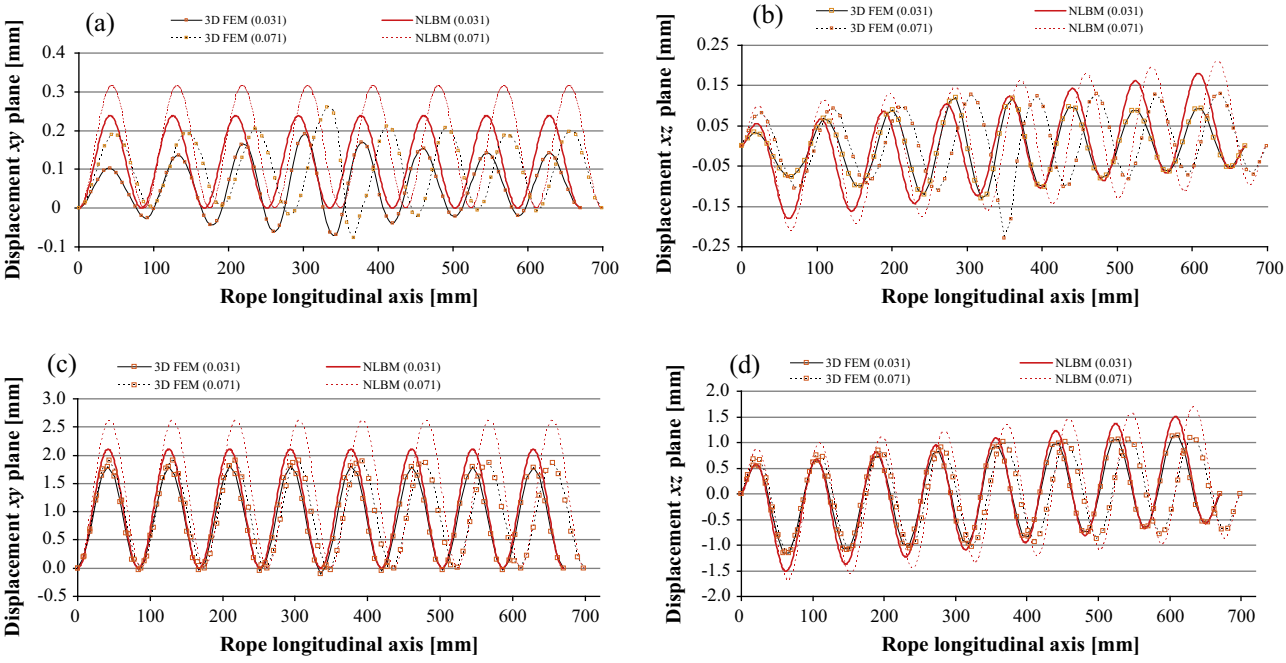

Fig. 12. Plane lateral deflection of ropes: (a) and (b) W_{136} rope; (c) and (d) W_{1234} rope.

parameter) can be used as a measure of the perturbation induced by the asymmetric damage distribution on rope initial configuration. Considering the maximum deflections values provided by the 3D FE and NLBM models and the rope axial strain range [0.012, 0.106] specified in Table 4, the ranges of this perturbation parameter defined by these two models are [0.00034, 0.0035] and [0.00027, 0.0046] respectively. As extensible discussed in this paper, the results given by these two models agree quite well between each other; thus, considering the range of the perturbation parameter values defined by the NLBM model (values defined by the 3D FE models is a subset of this range), it can be concluded that as the perturbation parameter values be small, initial rope configuration is slightly perturbed by the asymmetric damage distribution. Hence, for computational purposes, and also supported by the analyses presented in Fig. 5, the deformed configuration of rope components of the second layer can be accurately estimated by a first order circular helix curve. It is interesting to point out that the M-B model gives comparable results with both 3D FE and NLBM models only for ropes W_{136} and W_1 although much larger values of the perturbation parameter are estimated. In these cases, the overestimation and the underestimation of the tensile stress of the adjacent and opposite rope components to damage respectively (Figs. 8 and 9) compensate each other resulting in a good correlation among the predicted capacity curves (3D FE, NLBM, and M-B models) and with experimental data as discussed in Fig. 6a and b.

It is worth to mention that the computational efficiency of the proposed algorithm is very high relative to the results given by the 3D FE nonlinear simulations. For each point of the estimated capacity curves, considering all the damaged ropes analyzed, the required number of iterations to meet the convergence criterion (*Step 8* of the proposed algorithm) is less or equal than five. Although 3D FE nonlinear simulations provide a possibility for very precise analyses of damaged rope behavior, they require a couple of hours to complete them (compute an n-points capacity curve (n ranges from 30 to 100), stress/strain states, and deformed configuration of the rope of a 885,000 degrees of freedom models) on a standard multi-core processor computer (quad-core 3.4 GHz-16 Gb RAM) while the proposed algorithm needs less than one minute for the same analyses providing accurate results as previously commented. The robustness of the present algorithm is confirmed by the fact that all the capacity curves and deformed configurations associated to the damaged ropes analyzed, which accounts for a wide range of *IA* values, were accurately estimated (relative to 3D FE results and experimental data) and they converged after few iterations (less or equal than five) [30].

Although the proposed mechanical model was validated for small-scale one-level two-layer ropes, they are qualified to examine solely the impact of asymmetric damage distribution on rope response in which the results obtained can give an insight if the asymmetric damage distribution can be ignored in the analysis of damaged ropes. The associated iterative algorithm can be readily extended for the case of asymmetrically damaged multilayered one-level ropes (larger ropes), considering the appropriate value of the unbalanced transverse force as described in [16], if broken components belong to the outermost layer. If damage is localized in inner layers or the damaged rope has a multilevel geometry, interaction among rope components may induce strain localization around the damage zone making the response of the damaged rope length dependent as extensively discussed in [9,16,18] among others. In the latter, not only the damage distribution (degree of asymmetry) should be accounted for, but also the length of the rope, damage location within rope cross-section and rope length, and contact pattern between rope components.

Additionally, damage assessment guidelines require damage tolerance documentation of the rope components. For the particular example of a fiber rope of the parallel subrope type used for mooring applications, the residual strength of a damaged rope is estimated by using the summation principle in which rope behavior is determined by the behavior of a subrope which is formed by strands (small ropes) that can have helical construction. Mechanical damage occurs at strands level and the proposed model can be utilized to estimate their residual strengths for a variety of damage distribution in the absence of experimental data [31].

4. Conclusions

In this paper, a simplified mechanical model to account for the effect of asymmetric damage distribution to rope cross-section on overall static rope response is presented. In this model the asymmetric damaged rope is assumed to behave as a nonlinear beam with Bernoulli's kinematic hypothesis with uncoupled biaxial bending response (i.e., two uniaxial bending analyses), subjected to axial loading and a transverse uniform force resulting from the net radial force acting on rope cross-section due to the initial helical geometry of rope components along with the loss of cross-section symmetry. An efficient and robust iterative cross-sectional numerical algorithm is implemented to estimate rope capacity curve, stress and strain distributions throughout rope cross-section and rope geometry deformation for a prescribed axial displacement of the rope.

An extensive study is carried out on small-scale asymmetric damaged polyester ropes (ropes diameter equal to 6 mm) whose *IA* values range from 0.093 to 0.54 Predicted results given by the proposed model (NLBM) overestimate in a range of [8%, 12%] the residual strength and in less then 2% the failure axial strain relative to the results given by 3D FE nonlinear simulations. In terms of the rope geometry deformation, the asymmetric damaged rope subjected to tensile load laterally deflects inducing additional bending stresses in unbroken rope components. The NLBM model overestimates the maximum lateral defection in an average range of [12%, 20%] whereas predicted normal stress and strain values in unbroken rope components are bounded when compared with 3D FE results. As the value of the *IA* index increases, rope initial geometry perturbation increases as well, and consequently, an additional reduction over the percentage of loss of cross-sectional area in the residual rope strength occurs. The NLBM and 3D FE models, however, suggest that for *IA* values less than 0.44, rope residual strength can be satisfactory estimated based upon the net area effect model. Regarding to the rope failure axial strain, both models provide very similar results in which this parameter decreases as the *IA* value increases, reaching a maximum reduction around 8% (for $IA = 0.54$) relative to the intact rope value. Two linear models reported in the literature, included in this study for validation purposes of the proposed model, only provide accurate results in terms of the capacity curves and tensile stress (strain) developed by the unbroken rope components for ropes with low values of the *IA* index (less than 0.16); thus, the NLBM model is applicable with satisfactory results to ropes with greater degree of asymmetry.

Further comparisons with experimental data of bigger ropes (or rope components) are needed to verify the assumptions made and establish the range of applicability of the proposed model (NLBM). Additionally, while the NLBM can be used to obtain a reasonable estimate of the static response of asymmetric damaged ropes, improvements such as the evaluation of the effect of torsion on stress/strain distribution, comparative analyses with damaged ropes comprised of materials different than polyester, include the potential strain localization around the damage zone and the corresponding variation of the axial strain along the rope length due to frictional effects, and relative slippage among rope components due to rope curvature are still needed before it can be reliably used for detailed design calculations and to develop specific guidelines on damage evaluation and discard criteria. Despite these limitations, and based on the preliminary results presented in this paper and the lower computational cost than the 3D FE models involved, the proposed model seems to be a promising computational tool for estimating residual strengths and deformation capacities of asymmetric damaged ropes.

Acknowledgments

The authors would like to acknowledge and thank the sponsor of this work Department of Civil Engineering at University of Chile for its financial support.

Appendix A

Index of asymmetry

The index of asymmetry (*IA*) parameter is defined as [18]

$$IA = 1 - \frac{r_0 - e(\varepsilon)}{r_0 + e(\varepsilon)} \tag{A1}$$

where r_0 is the rope radius and $e(\varepsilon)$ is the distance from the centroid of the rope to the location of the center of stiffness of rope cross-section for a particular value of the axial rope strain ε. The expressions needed to compute the function $e(\varepsilon)$ are the following:

$$A = \sum_{n \in Q} A_n \tag{A2}$$

$$S_n = \frac{1}{A_n} \iint_{\Omega_n} \frac{d\sigma}{d\varepsilon} d\Omega \quad \text{for} \quad n \in Q \tag{A3}$$

$$x_n = \frac{1}{S_n A_n} \iint_{\Omega_n} \frac{d\sigma}{d\varepsilon} x' d\Omega \quad \text{for} \quad n \in Q \tag{A4}$$

$$y_n = \frac{1}{S_n A_n} \iint_{\Omega_n} \frac{d\sigma}{d\varepsilon} y' d\Omega \quad \text{for} \quad n \in Q \tag{A5}$$

$$S = \frac{1}{A} \sum_{n \in Q} S_n A_n \tag{A6}$$

$$x = \frac{1}{SA} \sum_{n \in Q} S_n A_n x_n \tag{A7}$$

$$y = \frac{1}{SA} \sum_{n \in Q} S_n A_n y_n \tag{A8}$$

$$e = e(\varepsilon) = \sqrt{x^2 + y^2} \tag{A9}$$

where n identifies rope components of the rope which are grouped in the subset Q; A_n (Ω_n) is the cross-sectional area of component n; S_n and S are the axial stiffness of the component n and rope respectively; (x_n, y_n) and (x, y) are the coordinates of the center of the stiffness of the component n and rope respectively. The discrete nature of the above equations is consistent with the discrete formulation of the proposed mechanical model (NLBM) as discussed in Section 2.2 of this paper.

B. Lanteigne's model

Lanteigne [13] studied the response of cables under static loading conditions that include any combination of tension, torsion and bending. The deformation geometry of the cable is linearized and the axial strain values of its components are linear dependent on axial elongation, axial rotation, and curvature specified for the

Table B1
Stiffness coefficients for Lanteigne's model.

$AE = \sum_{n=1}^{N} k_n A_n E_n \cos^3\theta_n + A_c E_c$	$JG = \sum_{n=1}^{N} k_n A_n E_n R_n^2 \sin^2\theta_n \cos\alpha_n + J_c G_c$
$k_{FM_T} = \sum_{n=1}^{N} k_n A_n E_n R_n \cos^2\theta_n \sin\theta_n$	$IE = \sum_{n=1}^{N} k_n A_n E_n \left(\frac{R_n^2 + r_n^2/2}{2}\right) \cos^3\theta_n + I_c E_c + \sum_{n=1}^{N}\sum_{i=1}^{k_n} A_n E_n B_{in}$
$k_{FM_B} = \sum_{n=1}^{N}\sum_{i=1}^{k_n} A_n E_n A_{in}$	$k_{M_T M_B} = \sum_{n=1}^{N}\sum_{i=1}^{k_n} A_n E_n A_{in} R_n \tan\theta_n$
$A_{in} = \frac{R_n^2 \cos^3\theta_n}{L_0 \tan\theta_n}\left[\cos\left(\frac{2\pi i}{k_n}\right) - \cos\left(\frac{2\pi i}{k_n} + \frac{L_0 \tan\theta_n}{R_n}\right)\right]$	$B_{in} = \frac{R_n^2 \cos^3\theta_n}{4L_0 \tan\theta_n}\left[\sin\left(\frac{4\pi i}{k_n}\right) - \sin\left(\frac{4\pi i}{k_n} + \frac{2L_0 \tan\theta_n}{R_n}\right)\right]$

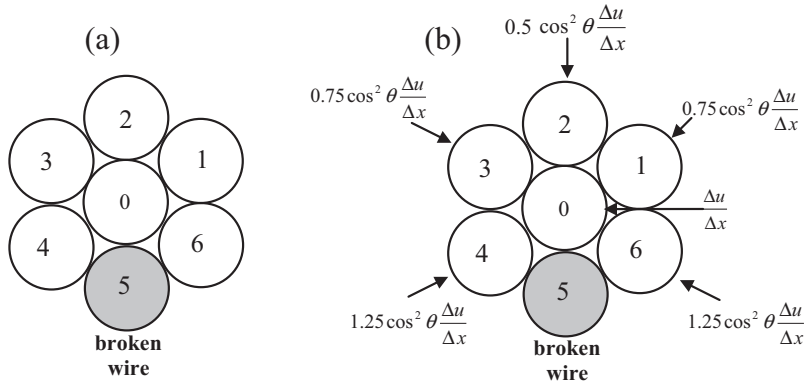

Fig. C1. (a) Damaged rope cross-section; (b) axial strain at each unbroken wire.

cable, assuming Bernoulli's kinematic hypothesis. Thus, the equilibrium equation for the cable is given by the following relation

$$\begin{bmatrix} F \\ M_T \\ M_B \end{bmatrix} = \begin{bmatrix} AE & k_{FM_T} & k_{FM_B} \\ k_{FM_T} & JG & k_{M_T M_B} \\ k_{FM_B} & k_{M_T M_B} & IE \end{bmatrix} \begin{bmatrix} \Delta u/L_0 \\ \Delta\omega/L_0 \\ \Delta\psi/L_0 \end{bmatrix} \tag{B1}$$

where F is the tensile load, M_T is the torsional moment, M_B is the bending moment, Δu is a uniform elongation, $\Delta\omega$ is the axial rotation angle, $\Delta\psi$ is the bending angle, and L_0 is the initial length of the cable. The stiffness coefficients are given in Table B1.

where the subscripts c and n refer to the core of the cable and to a particular layer of it, k_n is the number of component in layer n, A_n and E_n are the cross-section and Young's modulus of components in layer n respectively, θ_n is the helix angle of components in layer n, and R_n and r_n are the radius of layer n and radius of components that lay in layer n.

For an asymmetric damage distribution, the term k_{FMB} does not vanish. If the values of $\Delta u/L_0$ and $\Delta\omega/L_0$ are prescribed (displacement control analysis) and the value of M_B is equal to zero, the value of $\Delta\psi/L_0$ can be obtained from Eq. (B1). Performing a cross-sectional analysis, the axial strain ε_{in} and normal stress σ_{in} of the ith component of layer n are computed in terms of $\Delta u/L_0$, $\Delta\omega/L_0$, and $\Delta\psi/L_0$. Adding up (discrete formulation) the contributions from all unbroken components, the capacity curve of asymmetric damage rope can be estimated.

C. MacDougall and Barlett's model

MacDougall and Bartlett [15] proposed a mechanical model to include the effects of asymmetric damage to cross-section on the static response of a seven wire prestressing tendon (wire rope) utilized in posttensioned concrete structures. The development of this linear analytical model only considers the failure of a single outer wire (wire 5 (gray color) in Fig. C1a) and it is based on the assumption that the rope deflects laterally due to the fact that radial forces exerted on its core are not in equilibrium in the initial rope configuration. This lateral deflection is controlled by the new radial equilibrium configuration in which the rope develops a helix curve around its original longitudinal axial. Thus, for some rope components the helix radius increases and for others decreases inducing additional (positive and negative) axial elongation and local bending in them. The rope deflection (δ_p) perpendicular to its axis at a distance x from the wire break for a prescribed rope axial strain $\Delta u/\Delta x$ is given by

$$\delta_p(x) = \frac{1}{2}\frac{R_h}{\sin^2\theta}\left[\cos^2\theta\frac{\Delta u}{\Delta x} - \varepsilon_b(x)\right] \tag{C1}$$

where ε_b is the axial strain in the broken due to interwire friction, R_h is the helix radius, and θ is the helix angle. The axial strain value in each unbroken wire is given by (Fig. C1a)

$$\varepsilon_{4,6}(x) = \cos^2\theta\frac{\Delta u}{\Delta x} + \frac{\sin^2\theta}{R_h}\frac{\delta_p(x)}{2} \tag{C2}$$

$$\varepsilon_{1,3}(x) = \cos^2\theta\frac{\Delta u}{\Delta x} - \frac{\sin^2\theta}{R_h}\frac{\delta_p(x)}{2} \tag{C3}$$

$$\varepsilon_2(x) = \cos^2\theta\frac{\Delta u}{\Delta x} - \frac{\sin^2\theta}{R_h}\delta_p(x) \tag{C4}$$

where the first term of the above equations corresponds to the axial rope strain as if the rope were undamaged (rope geometry deformation linearized) and the second terms is related to the effect of the lateral rope deflection due to asymmetric damage distribution, Based on the above equations, the axial strain distribution within a damaged rope cross-section with one outer component broken is depicted in Fig. C1(b), considering that strain recovery does not occur (i.e., $\varepsilon_b = 0$). Knowing the strain field throughout damaged cross-section, normal stress field is computed through the constitutive law of the material and subsequently, accounting for the contribution of all unbroken components, the capacity curve of the damaged tendon is estimated.

References

[1] Foster GP. Advantages of fiber rope over wire rope. J Indus Text 2002;32:67–75.
[2] McKenna HA, Hearle JSW, O'Hear N. Handbook of fibre rope technology. Cambridge (England): Woodhead Publishing Ltd.; 2004.
[3] Chaplin CR. The fatigue and degradation mechanisms of hoisting ropes. In: Hoist and Haul conference, Perth, Australia; 2005.

[4] Hankus J. Safety factor for hosting rope weakened by fatigue cracks in wires. In: Organisation Internationale pour l'Etude de l'Endurance des Cables (OIPEEC), Round Table Conference, June, Krakow; 1981.
[5] Cholewa W, Hansel J. The influence of the distribution of wire rope faults on the actual breaking load. In: Organisation Internationale pour l'Etude de l'Endurance des Cables (OIPEEC), round table conference, Krakow, Poland; June 1981.
[6] Chaplin CR, Tantrum N. The influence of wire break distribution on strength. In: Organisation Internationale pour l'Etude de l'Endurance des Cables (OIPEEC). Round table conference, Glasgow, Scotland; June 1985.
[7] Cholewa W. Wire fracture and weakening of wire rope. In: Wire rope discard criteria: round table conference. Swiss Federal Institute of Technology (ETH), Institute of Lightweight Structures and Ropeways, Zurich, Switzerland; September 1989.
[8] Oplatka G, Roth M. Relation between number and distribution of wire breaks and the residual breaking force. In: OIPEEC round table conference on wire rope discard criteria, Zurich; 1989.
[9] Evans JJ, Ridge IML, Chaplin CR. Wire failures in ropes and their influence on local wire strain behavior in tension–tension fatigue. J Strain Anal 2001;36(2):231–44.
[10] Li D, Miyase A, Williams JG, Wang SS. Damage tolerance of synthetic- fiber mooring ropes: small-scale experiments and analytical evaluation of damaged subropes and elements. Technical report, CEAC-TR-03-0101, University of Houston; 2002.
[11] Ward EG, Ayres RR, Banfield S, O'Hear N, Smith CE. Experimental investigation of damage tolerance of polyester ropes. In: Fourth international conference on composite materials for offshore operations, Houston, TX, USA; 2005.
[12] Flory J. Assessing strength loss of abraded and damaged fiber rope. In: OCEANS 2008 – MTS/IEEE Kobe, Japan; 2008.
[13] Lanteigne J. Theoretical estimation of the response of helically armoured cables of tension, torsion, and bending. J Appl Mech 1985;52(2):423–32.
[14] MacDougall C, Bartlett F. Mechanical model for unbonded seven-wire tendon with symmetric wire breaks. J Eng Mech 2005;131(12):1239–47.
[15] MacDougall C, Bartlett F. Mechanical model for unbonded seven-wire tendon with single broken wire. J Eng Mech 2006;132(12):1345–53.
[16] Beltran JF, Williamson EB. Numerical simulation of damage localization in polyester mooring ropes. J Eng Mech 2010;136(8):945–59.
[17] Beltran JF, Williamson EB. Numerical procedure for the analysis of polyester damaged ropes. Eng Struct 2011;33(5):1698–709.
[18] Beltran JF, Vargas D. Effect of broken rope components distribution throughout rope cross-section on polyester rope response: numerical approach. Int J Mech Sci 2012;64:32–46.
[19] Leech CM, Hearle JWS, Overington MS, Banfield SJ. Modeling tension and torque properties of fibre ropes and splices. In: Proc., 3rd Int. offshore and polar engineering conf., ISOPE, Singapore; 1993.
[20] Beltran JF, Williamson EB. Investigation of the damage-dependent response of mooring ropes. J Eng Mech 2009;135(11):1237–47.
[21] Mandell JF. Modelling of marine rope fatigue behavior. Text Res J 1987;57(6):318–30.
[22] Wu H-C, Seo MH, Backer S. Structural modeling of double-braided synthetic fiber ropes. Text Res J 1995;65:619–31.
[23] Hjelmstad K. Fundamentals of structural mechanics. New York (USA): Springer; 2005.
[24] Papailiou KO. On the bending stiffness of transmission line conductors. IEEE Trans Power Del 1997;12(4):1576–83.
[25] Costello GA. Theory of wire ropes. New York (USA): Springer-Verlag; 1990.
[26] Van den Heuvel CJM, Heuvel HM, Faasen WA, Veurink J, Lucas LJ. Molecular changes of PET yarns during stretching measured with rheo-optical infrared spectroscopy and other techniques. J Appl Polym Sci 1993;49:925–34.
[27] Ghoreishi S, Messager T, Cartraud P, Davies P. Validity and limitations of linear analytical models for steel wire strands under axial loading, using 3D FE model. Int J Mech Sci 2007;49:1251–61.
[28] Kreyszig E. Differential geometry. New York (USA): Dover; 1991.
[29] De Vico E. Efectos de la distribución asimétrica de daño en la sección transversal de un cable: modelación numérica. Thesis Civil lEngineering, University of Chile, Chile (Spanish); 2013.
[30] Ramirez N. Efectos del daño asimétrico en la capacidad residual de cables con geometría multicapa-multinivel: modelación numérica. Chile (Spanish): Thesis Civil Engineering, University of Chile; 2015 [in press].
[31] Ahjem V, Colby C, Flory J, Lee M, Petruska D. Fiber rope damage assessment and acceptance criteria-new guideline. USA: Offshore Technology Conference, OTC; 2004.